A numerical study on the blade-vortex interaction of a two-dimensional Darrieus-Savonius combined vertical axis wind turbine

Pan, Jingna; Ferreira, Carlos; van Zuijlen, Alexander

DOI
10.1063/5.0174394

Publication date
2023

Document Version
Final published version

Published in
Physics of Fluids

Citation (APA)
Pan, J., Ferreira, C., & van Zuijlen, A. (2023). A numerical study on the blade-vortex interaction of a two-dimensional Darrieus-Savonius combined vertical axis wind turbine. *Physics of Fluids*, *35*(12), Article 125152. https://doi.org/10.1063/5.0174394

Physics of Fluids

RESEARCH ARTICLE | DECEMBER 28 2023

A numerical study on the blade–vortex interaction of a two-dimensional Darrieus–Savonius combined vertical axis wind turbine

Special Collection: Flow and Civil Structures

Jingna Pan (潘静娜) ; Carlos Ferreira ; Alexander van Zuijlen

Physics of Fluids 35, 125152 (2023)
https://doi.org/10.1063/5.0174394

Physics of Fluids ARTICLE pubs.aip.org/aip/pof

A numerical study on the blade–vortex interaction of a two-dimensional Darrieus–Savonius combined vertical axis wind turbine

Cite as: Phys. Fluids **35**, 125152 (2023); doi: 10.1063/5.0174394
Submitted: 30 August 2023 · Accepted: 6 December 2023 ·
Published Online: 28 December 2023

Jingna Pan (潘静娜),[a] Carlos Ferreira, and Alexander van Zuijlen

AFFILIATIONS

Faculty of Aerospace Engineering, Delft University of Technology, Kluyverweg 1, 2629 HS Delft, The Netherlands

Note: This paper is part of the special topic, Flow and Civil Structures.
[a]**Author to whom correspondence should be addressed:** J.Pan-1@tudelft.nl

ABSTRACT

To investigate power losses of a Darrieus–Savonius combined vertical axis wind turbine (hybrid VAWT) associated with the interaction between blades and wake, it is crucial to understand the flow phenomena around the turbine. This study presents a two-dimensional numerical analysis of vortex dynamics for a hybrid VAWT. The integration of a Savonius rotor in the hybrid VAWT improves self-starting capability but introduces vortices that cause transient load fluctuations on the Darrieus blades. This study attempts to characterize the flow features around the hybrid VAWT and correlate them with the Darrieus blade force variation in one revolution. Results demonstrate the capability of numerical modeling in handling a wide range of operational conditions: the relevant position of Savonius and Darrieus blades (attachment angle $\gamma = 0^\circ - 90^\circ$) and Savonius' tip speed ratio λ_S (0.2–0.8, varied Savonius' rotational speed). The torque increase in the Darrieus blade in hybrid VAWT (compared to a single Darrieus rotor) due to the appearance of the vortex shedding from the advanced Savonius blade is independent of the attachment angle and tip speed ratio. Apart from start-up and power performances of the hybrid VAWT, the most rapid force fluctuation is identified when the Darrieus blade interacts with Savonius' wake at $\gamma = 0^\circ$ and $\lambda_S = 0.8$, which is considered undesirable. Furthermore, attachment angles of 60° and 90° exhibit better power coefficients compared to those of 0° and 30° for the hybrid VAWT. This study contributes to a comprehensive understanding of flow dynamics in hybrid VAWTs, revealing the correlation between torque variation and vortex development.

I. INTRODUCTION

Vertical axis wind turbines (VAWTs) are not sensitive to the wind direction. Therefore, they can operate without active control. This great feature makes this turbine attractive to use in urban areas, where the wind direction changes continuously. They are categorized into two types: lift-driven Darrieus and drag-driven Savonius. There are abundant studies on the two types of turbines, and some notable results are listed in Table I, showing the type of the rotor, minimum (and maximum) operational tip speed ratio λ_{min} (and λ_{max}), and corresponding peak power performance $c_{p_{max}}$. Savonius rotor has a good self-starting performance.[1–3] However, it has a low power efficiency. Darrieus rotor can achieve a maximum power coefficient of up to 0.3–0.5.[1,4–7] However, it cannot self-start in practice.

Darrieus and Savonius rotors have their advantages and disadvantages. The Darrieus–Savonius combined vertical axis wind turbine (hybrid VAWT) combines the advantages and disadvantages of both types of turbines and offers some unique strengths and weaknesses. The sketch of the hybrid VAWT is depicted in Fig. 1. For their strengths, the hybrid VAWT can produce more torque for self-starting compared to a Darrieus turbine, beneficial from the existence of Savonius.[1,8–10] In addition, it has a wide operation range and can generate power at either low or high inflow speeds, making it well-suited for locations with variable inflow conditions.[11,12] For their weaknesses, the hybrid VAWT generates less power per unit of rotor area compared to a Darrieus turbine.[1,8–12] The power and start-up performances of hybrid VAWT are affected by the wake introduced by the inner Savonius. The change in the wake patterns of hybrid VAWT has limited the amount of wind energy that can be captured and converted into mechanical energy. To study the effect of these limitations on the hybrid VAWT, engineers and researchers have investigated flow

TABLE I. Operational conditions of Darrieus and Savonius rotors.

Author	VAWT	λ_{min}	λ_{max}	$c_{p_{max}}$
Hosseini and Goudarzi[1]	3-bladed Darrieus	1	5	0.48
Castelli *et al.*[4]	3-bladed Darrieus	1.43	2.7	0.31
Wang *et al.*[5]	2-, 3-, and 4-bladed Darrieus	∼ 0.8	∼ 4	∼0.4
Gosselin *et al.*[6]	3-bladed Darrieus	1.8	5.2	0.36
Shao *et al.*[7]	2-bladed Darrieus	2	∼ 7	0.38
Hosseini and Goudarzi[1]	Bach-type Savonius	∼ 0.6(self-start)	∼ 1	0.27
Wekesa *et al.*[2]	Three-bladed Savonius	∼ 0.2(self-start)	∼1.3	0.18
Fatahian *et al.*[3]	Two-bladed vented Savonius	0.4(self-start)	1	0.275

physics around the hybrid VAWT and developed different designs to improve the power performance of the hybrid VAWT.

The effect of different parameters on the performance of the hybrid VAWT has been investigated in many studies. Roshan *et al.*[13] investigated the effects of the arc angle of the Savonius blades Φ, the overlap ratio $\varepsilon = \frac{e}{R_S}$, and the Savonius blade curvature $\alpha = \frac{R_1}{R_2}$ on the performance of the turbine. In each of the three variables, $\varepsilon = 0.25$, $\alpha = 0.25$, and $\Phi = 150°$ were proposed in order to optimize the self-starting performance and extend the operational range of the hybrid VAWT. In the study of Asadi and Hassanzadeh,[14] the performance of a hybrid VAWT constructed by a two-bladed Darrieus rotor as the external rotor and a two-bladed Savonius rotor as the internal rotor was assessed numerically. It was demonstrated that the tip speed ratio of hybrid VAWT λ_{hybrid} strongly influenced the choice of an appropriate attachment angle γ (relevant position of Savonius and Darrieus blades). The power coefficient of the hybrid VAWT with an attachment angle of 45° was the optimal case for $\lambda_{hybrid} = 1.5$ and 2.5. However, their study did not discuss the flow fields in detail. Kyozuka[15] conducted a series of experiments to study the hydrodynamic characteristics of a Darrieus–Savonius rotor. They found that the attachment angle was important in the starting performances of the hybrid VAWT. However, the power coefficient was decreased to 70% of the separate Darrieus VAWT. Liang[8] studied the effects of the radius ratio and attachment angle on the performance of a hybrid VAWT.

A few studies have been conducted to understand the blade–vortex interaction around a single VAWT. Bangga[16] investigated the effects of airfoil thickness on the dynamic stall characteristics of high-solidity VAWTs. The results showed that the leading-edge vortex bubble was the main cause of the power loss for high-solidity VAWTs, and the leading-edge vortex strength and radius were reduced with increasing airfoil thickness. It also reported that the interaction between the blade and wake discouraged perfect periodicity when the turbine operates at a small tip speed ratio. Wang[17] investigated the power performance of vertical axis wind turbines with different airfoil shapes and analyzed the interaction between vortex and wind turbine blades.

The blade–vortex interaction in the hybrid VAWT is more complex compared to the single VAWT. This complexity arises due to the presence of the Savonius rotor and its interaction with the Darrieus blades.[9,18–20] The challenge of optimizing the hybrid VAWT requires a parametric study, e.g., the radius ratio, the attachment angle, and the tip speed ratio of the hybrid VAWT. Several studies have already been published to evaluate the effects of these parameters on the aerodynamic force of the hybrid VAWT. Liu *et al.*[21] conducted a systematic

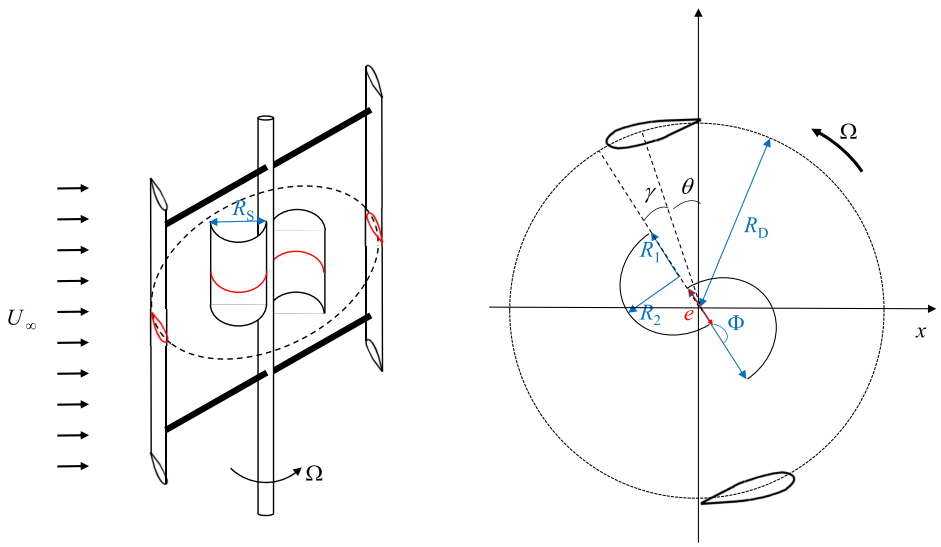

FIG. 1. Sketch of hybrid VAWT (Left: 3 D structure, right: top view).

study about the effects of the moment of inertia and radius ratio on the self-starting capability and power efficiency. Results showed that the hybrid VAWT with a small-size modified Savonius rotor ($\frac{R_D}{R_S} = 3.5$) can generate a higher maximum power coefficient ($c_{p_{max}} = 0.41$) compared to the hybrid VAWT with a large-size Savonius rotor ($\frac{R_D}{R_S} = 2.33$, $c_{p_{max}} = 0.375$). Kumar[18] optimized the Savonius rotor diameter to maintain the power coefficient of the Darrieus rotor in the hybrid VAWT. The interaction between the closed configuration Savonius rotor and the flow resulted in the formation of von Karman vortices. These vortices then interacted with the Darrieus blades, causing flow detachment. Through their analysis, it has been determined that an optimal diametrical ratio of 3 led to the highest power coefficient for the Darrieus rotor. By integrating a compact Savonius rotor within the hybrid VAWT, one can harness its self-starting capabilities while mitigating potential flow structure interactions that might affect turbine performance. Saini and Saini[22] numerically studied the effect of radius ratio and attachment angle on the performance of the hybrid hydrokinetic turbine. The pressure and velocity contours were analyzed for hybrid VAWT at unvaried conditions $\frac{R_D}{R_S} = 5$ and $\gamma = 30°$. The power and start-up performances were discussed for different operating conditions ($U_\infty = 0.5$–2.5 m/s, $\lambda = 2$–3.6, $\gamma = 0° - 90°$, $\frac{R_D}{R_S} = 3$–5). Results showed that the power coefficient decreased as the radius ratio increased and the maximum starting torque was found at $\frac{R_D}{R_S} = 5$, $\gamma = 30°$ and 60°. The aforementioned investigations drive us to conceptualize a hybrid VAWT with a reduced-size Savonius rotor.

These studies have explored various aspects related to flow structures and turbine performance individually. There exists a gap in our understanding regarding the variation of blade force in response to vortex dynamics. In a word, a comprehensive discussion on the correlation between flow structures and turbine performances has not been thoroughly addressed yet. To address this gap, further studies are required to conduct in-depth analysis that correlate flow structures with specific turbine performance metrics. It involves identifying and quantifying the key flow features, such as vortices, wake interactions, turbulence patterns, and their direct influence on critical turbine parameters, such as power output and torque. This study is an extended work in terms of investigating the correlation between blade–vortex interaction and blade force variation.

The characterization and correlation of the vortex dynamics and blade torque play an important role in the design phase of the hybrid VAWT. In addition, the study of vortex dynamics might be useful for future studies on the engineering model of the hybrid VAWT. A parametric study of hybrid VAWT is conducted to better understand the flow mechanisms and performances of the hybrid VAWT. The presence of the Savonius rotor affects not only the rotor performance but also the downstream wake pattern. Their correlations are explored based on the Savonius-related parameters: attachment angle (position of Savonius blade relative to Darrieus blade) and Savonius' tip speed ratios (varied Savonius' rotation speed) in the current work.

Over the past few years, the growth in computational capabilities has paved the path for tackling the computation of VAWTs using computational fluid dynamics (CFD). However, these simulations require an expensive computational investment, resulting in this method still impractical for design objectives. As a result, researchers have turned to simplified two-dimensional (2 D) models, which significantly reduce computational demands. The two-dimensional (2 D) blade-resolved simulations can capture the primary vortex dynamics and yield comparable trends in quantitative results for VAWTs (e.g., streamwise velocity and blade force).[23–25] Fatahian *et al.*[3] investigated the flow dynamics and rotor performance of a vented Savonius using 2 D unsteady simulation in ANSYS Fluent. The numerical results of the rotor aerodynamic performance exhibited similar trends to the experimental results.[26] Li *et al.*[27] studied the wave–turbine interaction of a Savonius hydrokinetic turbine using 2 D simulations in STAR-CCM+. The simulated wave evolution was validated against the theoretical and experimental values. Results indicated that the turbine diameter and blade number will affect the turbine efficiency. Vigneswaran and VishnuKumar[28] explored the effect of co-flow jet (CFJ) velocity, the injection height, and the injection mass flow rate on the aerodynamic coefficient of a 2 D co-flow jet (CFJ) airfoil in ANSYS Fluent. Results showed that the jet velocity played a significant role in affecting the aerodynamic coefficient of CFJ airfoils. The aforementioned geometrical parameter (attachment angle) and operational parameter (Savonius' tip speed ratio) are all 2 D parameters. With the aim of characterizing the flow features of the hybrid VAWT and conducting a cost-effective parametric study, 2 D simulations are considered sufficient in this study.

This paper is structured as follows. The numerical procedure is presented in Sec. II. The effects of attachment angle and Savonius' tip speed ratio on the hybrid VAWT performances and correlation of vortex dynamics and blade torque are analyzed in Sec. III. The main results are concluded in Sec. IV, followed by the mesh independence study and meshing strategy of single rotors in Appendixes A and B.

II. NUMERICAL PROCEDURE

A. Geometry of the hybrid turbine

The 2 D simulations are conducted in OpenFOAM.[29] The hybrid VAWT consists of Savonius blades inside and Darrieus blades mounted on the same rotation axis. The Savonius rotor has two semicircle blades without an overlap and a gap distance, which is a relevant work to Ref. 23. The Darrieus blades are chosen as NACA0021, corresponding to the work in Ref. 30. The geometrical and operational parameters of the hybrid VAWT are shown in Table II, where $\lambda_S = \frac{\omega_S R_S}{U_\infty}$ and $\lambda_{hybrid} = \lambda_D = \frac{\omega_D R_D}{U_\infty}$.

TABLE II. Detailed geometrical and operational information of the hybrid turbine.

Parameter	Value/Specification	Unit
Radius of inner Savonius R_S	0.148	m
Radius of outer Darrieus R_D	0.74	m
Tip speed ratio of inner Savonius λ_S	[0.2, 0.4, 0.6, 0.8]	···
Tip speed ratio of outer Darrieus λ_D	[2.4, 2.9, 3.7, 4.0, 4.2]	···
Tip speed ratio of hybrid VAWT λ_{hybrid}	[1.0, 2.4, 2.9, 3.7, 4.0, 4.2]	···
Blade of inner Savonius	Semicircle	···
Blade of outer Darrieus	NACA0021	···
Chord length of outer Darrieus	0.075	m
Attachment angle γ	[0, 30, 60, 90]	°

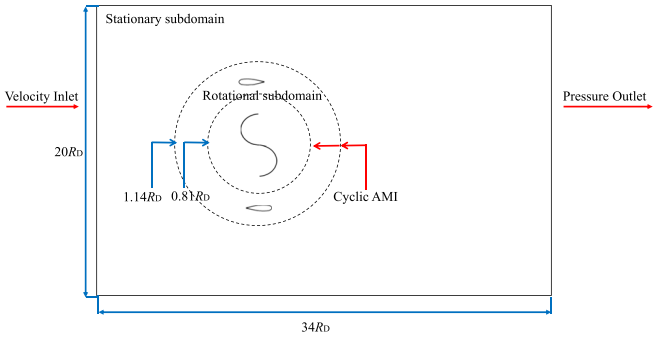

FIG. 2. Computational domain and boundary conditions (Not true to scale).

The attachment angle γ and the tip speed ratio of Savonius λ_S are varied to conduct an in-depth study that characterizes the flow structure relevant to blade force variation. It is worth noting that λ_S is changed by varying its rotation speed instead of radius because the operational condition is more convenient to control than the geometrical condition during turbine operation.

B. Turbulence model and boundary conditions

The unsteady, incompressible Reynolds-averaged Navier–Stokes (URANS) equations are solved by PIMPLE [a combination of PISO (pressure-implicit split-operator) and SIMPLE (semi-implicit method for pressure-linked equations)] algorithm to improve the numerical accuracy upon multi sub-iterations. The governing equations include the conservation of mass and the conservation of momentum, which are expressed by Eqs. (1) and (2), respectively. u_i and u_j represent the velocity components in the i and j directions. The model of Eq. (2) reflects the fact that the flow around the rotating blade is turbulent, and closure of the URANS equations is achieved using the shear stress transport (SST) k-w turbulence model. This turbulence model can predict boundary layers under strong adverse pressure gradients and has been validated in the application of wind turbines with good results.[31,32] It predicts accurate results for separation flows.[33,34] The turbulent kinetic energy k and dissipation rate w are expressed as Eqs. (3) and (4),[35,36] respectively. In Eqs. (3) and (4), the generation of the turbulent kinetic energy and dissipation rate are represented by G_w and G_k, respectively. Γ_k and Γ_w represent the effective diffusivity of k and w, respectively. Y_w and Y_k are the dissipation of w and k, respectively. S_k and S_w are source terms. D_w is the blending function for the standard k-ε and standard k-w model[31,32]

$$\frac{\partial u_i}{\partial x_i} = 0, \tag{1}$$

$$\rho\frac{\partial u_i}{\partial t} + \rho\frac{\partial (u_i u_j)}{\partial x_j} = -\frac{\partial p}{\partial x_i} + \frac{\partial}{\partial x_j}\left[(\mu + \mu_t)\frac{\partial u_i}{\partial x_j}\right], \tag{2}$$

$$\frac{\partial (\rho k)}{\partial t} + \frac{\partial (\rho k u_i)}{\partial x_i} = \frac{\partial}{\partial x_j}\left(\Gamma_k \frac{\partial k}{\partial x_j}\right) + G_k - Y_k + S_k, \tag{3}$$

$$\frac{\partial (\rho w)}{\partial t} + \frac{\partial (\rho w u_i)}{\partial x_i} = \frac{\partial}{\partial x_j}\left(\Gamma_w \frac{\partial w}{\partial x_j}\right) + G_w - Y_w + D_w + S_w. \tag{4}$$

The schematic of the computational domain and boundary conditions is depicted in Fig. 2. The mesh details of the computational domain are shown in Fig. 3. The inflow comes from left to right of the computational domain; the boundary conditions of the computational domain are determined as follows:

- Inlet boundary: The inlet wind speed is equal to the freestream velocity.
- Outlet boundary: The given outlet pressure is the standard ambient pressure.
- Wall boundary: No-slip rotating wall boundary conditions are used along the blade surfaces.

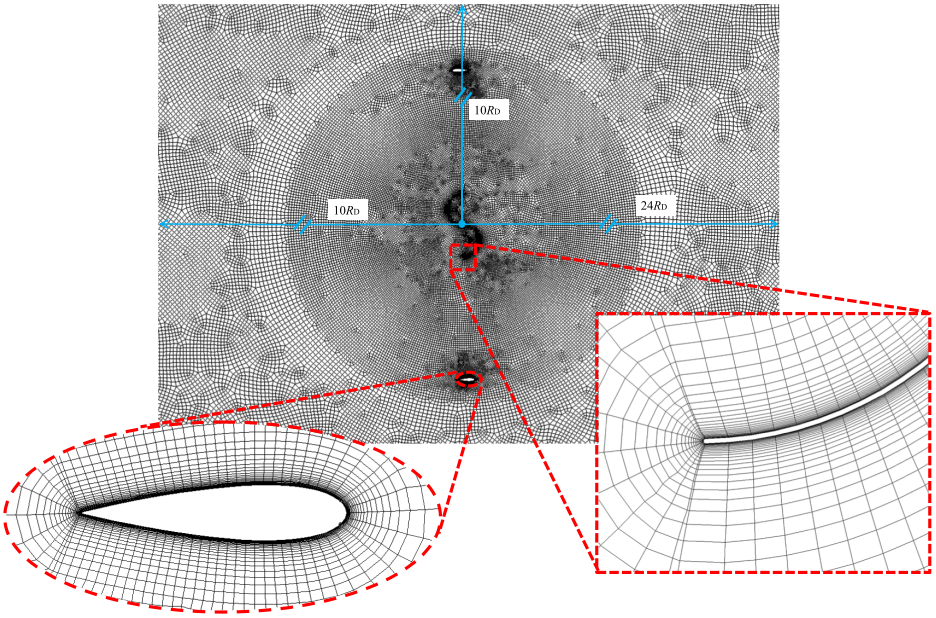

FIG. 3. Mesh generation in the computational domain.

TABLE III. Power coefficient of hybrid VAWT from different mesh configurations, $\lambda_{hybrid} = 4.0$, $U_\infty = 4.01$ m/s, and $\gamma = 0°$.

Mesh	Fine	Medium	Coarse
Number of cells	1.99×10^5	1.68×10^5	1.40×10^5
Darrieus blade discretization	102	76	66
Savonius blade discretization	304	220	140
Power coefficient c_p	0.3753	0.3694 (−1.57%)	0.3651 (−2.72%)

- Slip plane: There is a sliding mesh interface between the moving and the stationary grids. CyclicAMI boundary condition is employed to couple conditions between a pair of patches that share the same outer bounds. This boundary condition allows the physical rotation of the rotation subdomain. And the force variation would be well evaluated.

C. Mesh independence study

A mesh independence study of a hybrid VAWT with two semicircular Savonius blades and two Darrieus blades is conducted to determine the appropriate cell size. Three mesh configurations (coarse, medium, and fine) are involved with cell numbers of 1.99×10^5, 1.79×10^5, and 1.40×10^5, respectively. The computational domain and the first row's cell height are identical to the single-rotor case, as shown in Appendixes A and B. The simulation residual and time step size are selected as 1×10^{-5} and 0.24°/step to be consistent with the single Savonius and Darrieus simulations, respectively. The values of maximum skewness of the three mesh configurations are 0.70, 0.64, and 0.67, respectively. The average dimensionless wall distance y^+ is below one. The power coefficients from different mesh configurations and mesh details are shown in Table III. The variations of the power coefficient are depicted in Fig. 4. The power coefficients of the hybrid VAWT have a similar trend over the three mesh configurations. The fluctuations at $\theta = 60° - 120°$ and $\theta = 240° - 300°$ are attributed to the presence of Savonius' wake. This work will focus on torque fluctuation in response to the wake. The average power coefficients in Table III show that the medium mesh configuration yields reasonably accurate results with a 1.57% difference from the fine mesh configuration. To ensure cost-effective computations, a medium mesh is employed in the subsequent analysis.

D. Time independence study

A time independence study for the hybrid VAWT has been conducted to verify the stability of the simulation. Azimuthal increments $d\theta$ of 0.06°, 0.12°, 0.24°, 0.48°, 0.96°, and 4.8° are applied, and the power coefficients c_p are shown in Table IV. An Azimuthal increment of 4.8° tends to underestimate c_p by 5.1% compared to 0.06°. Among cases with $d\theta \leq 0.96°$, a negligible difference in c_p is observed. The comparison shows that $d\theta = 0.24°$ is a cost-effective choice in this study.

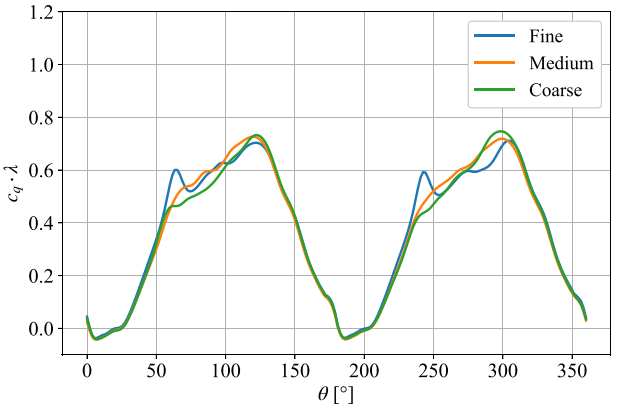

FIG. 4. Power coefficient variation for hybrid VAWT with different mesh configurations, $\gamma = 0°$, $\frac{R_0}{R_s} = 5.0$, $\lambda_{hybrid} = 4.0$.

E. Sensitivity study

The sensitivity study based on the computational domain size has been conducted. The distance between the rotor and the domain outlet is varied from $18R_{hybrid}$, $24R_{hybrid}$ to $30R_{hybrid}$. The power coefficients of hybrid VAWT for computational domains with varied outlet distances are listed in Table V. The difference between c_p for hybrid VAWT with an outlet distance of $18R_{hybrid}$ and $30R_{hybrid}$ is about 13.02%. This deviation drops to 0.43% for the hybrid VAWT with an outlet distance of $24R_{hybrid}$. Therefore, the distance between the rotor and the domain outlet is chosen as $24R_{hybrid}$.

Another sensitivity study examines the impact of varying numbers of revolutions on the average results. By systematically altering this parameter, we assess its influence on the power performances of the hybrid VAWT. This analysis provides insights into the stability and reliability of the findings, helping determine the optimal number of revolutions for obtaining consistent and representative results. The power coefficient variation in one cycle for different numbers of revolution is shown in Fig. 5. It is observed that the power coefficient tends to have an identical variation if more revolutions are taken into account. The mean power coefficient against different revolutions and different numbers of revolutions is depicted in Fig. 6. Due to the complex turbulence around the hybrid VAWT, the mean power coefficient of the single revolution fluctuates between 0.36 and 0.38. The mean power coefficient of several revolutions tends to converge at a magnitude of 0.37 when the 10th to 17th revolutions are averaged. In this

TABLE IV. Power coefficient of hybrid VAWT from different azimuthal increments, $\lambda_{hybrid} = 4.0$, $U_\infty = 4.01$ m/s, and $\gamma = 0°$.

Azimuthal increment $d\theta$	0.06°	0.12°	0.24°	0.48°	0.96°	4.8°
Time step size dt (s)	4.83×10^{-5}	9.66×10^{-5}	1.932×10^{-4}	3.864×10^{-4}	7.728×10^{-4}	3.864×10^{-3}
Power coefficient c_p	0.3693	0.3693	0.3694	0.3693	0.3693	0.3504

TABLE V. Power coefficient of hybrid VAWT from different distances between the rotor and domain outlet, $\lambda_{hybrid} = 4.0$, $U_\infty = 4.01$ m/s, and $\gamma = 0°$.

Distance between the rotor and outlet	$18R_{hybrid}$	$24R_{hybrid}$	$30R_{hybrid}$
Power coefficient c_p	0.3227 (−13.02%)	0.3694 (−0.43%)	0.3710

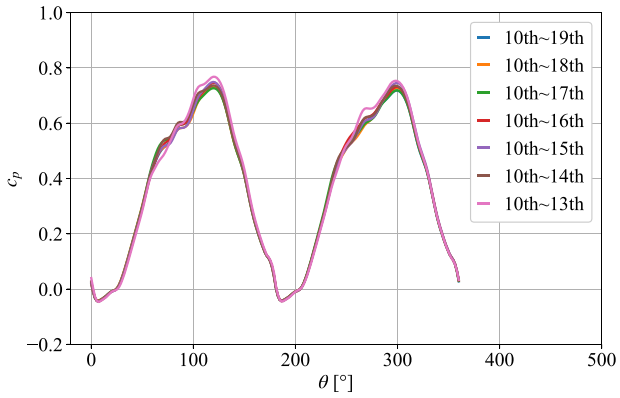

FIG. 5. Power coefficient variation for hybrid VAWT in different numbers of revolution, $\gamma = 0°$, $\frac{R_D}{R_S} = 5.0$, $\lambda_{hybrid} = 4.0$.

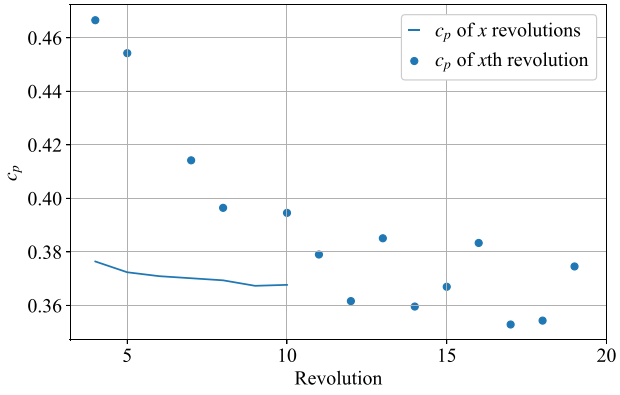

FIG. 6. Mean power coefficient for hybrid VAWT in different revolutions and different numbers of revolutions, $\gamma = 0°$, $\frac{R_D}{R_S} = 5.0$, $\lambda_{hybrid} = 4.0$ (x axis for solid line: Total number of revolution considered for the mean power coefficient).

work, eight revolutions (10th–17th) are used for the calculation of the mean power coefficient for the hybrid VAWT.

III. RESULTS AND DISCUSSION

The start-up and power performances of a hybrid VAWT with a two-bladed Savonius and two-bladed Darrieus are estimated in this section. The effects of the attachment angle and the inner Savonius' tip speed ratio (varied Savonius' rotation speed) on the power performances of the hybrid VAWT are analyzed in this section. To further understand the flow physics of the hybrid VAWT, the Darrieus blade

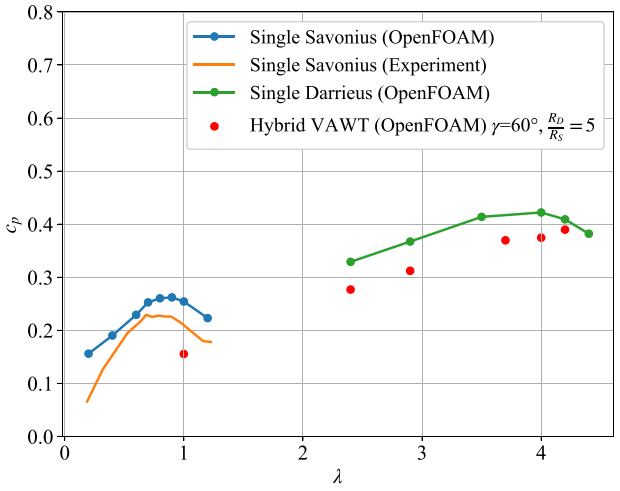

FIG. 7. Power coefficient of single Savonius, single Darrieus, and hybrid VAWT.

force variation is correlated with the wake patterns, which will provide insights into the hybrid VAWT design.

Power performances of single Savonius, single Darrieus, and hybrid VAWT with various tip speed ratios are shown in Fig. 7. The CFD simulations of Savonius have been validated against experimental results in Ref. 37. The numerical results of Darrieus are validated in Appendix B. There is a lack of experimental investigation on the studied hybrid VAWT, but a similar numerical method and meshing strategy have been applied to the hybrid VAWT. The sensitivity study of the hybrid VAWT indicates that the simulation stability and convergence are sufficient. The single Savonius results from experiments are lower than those from CFD simulations. This can be attributed to the absence of 3 D effects (e.g., tip vortices), which are not discussed in this work.

A. Start-up performance

As shown in Fig. 7, the single Savonius can operate at a tip speed ratio lower than 1, but the single Darrieus has a higher power output at high tip speed ratios. As studied in Refs. 18 and 21, reducing the size of Savonius would increase the maximum power performance of the hybrid VAWT. In Fig. 7, the optimum tip speed ratio of the single Darrieus is about five times that of the single Savonius. So, the radius of the outer Darrieus part is selected as five times that of the inner Savonius part in the baseline hybrid VAWT to gain optimum power for the combined configuration as well as a good start-up performance.

The comparison of the torque coefficients for the single Savonius and Savonius in hybrid VAWT is shown in Fig. 8. The variations of torque coefficient with the tip speed ratio have the same trend: torque coefficient decreases with the increasing tip speed ratio. However, the torque coefficient of Savonius in hybrid VAWT is lower than that of single Savonius due to the velocity deficit caused by the rotor rotating. The rotation of the hybrid VAWT leads to a high induction to the flow field, so the performance of the Savonius (or Darrieus) part in the hybrid VAWT is different from that of the single rotor with the same operational conditions. Since the Darrieus is the major contributor to the power generation in the hybrid VAWT, its tip speed ratio remains

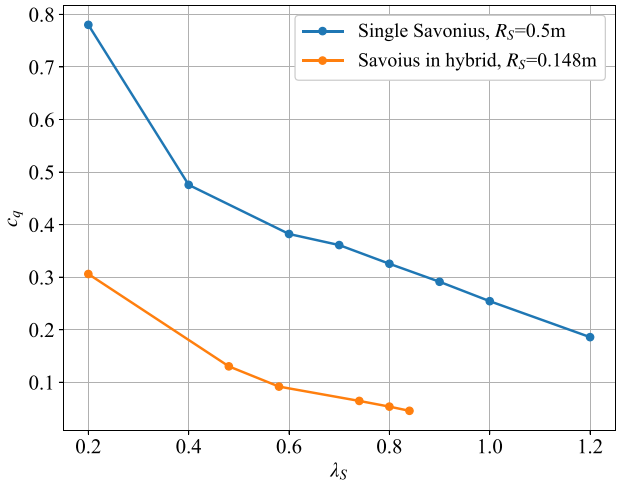

FIG. 8. Torque coefficients of single Savonius and Savonius in hybrid VAWT.

at optimal condition, and the effect of Savonius' tip speed ratio on the performance of the hybrid VAWT is studied. Savonius' tip speed ratio is varied by changing the rotation speed of Savonius. Their flow features and blade forces are analyzed in Sec. III B 2.

As the Savonius blade position at static conditions influences the static torque,[38] the static torque of the Savonius blade in hybrid VAWT is investigated under varied angular positions. The static torque coefficients of the single Savonius and Savonius in hybrid VAWT are compared in Fig. 9. It is observed that the Savonius in hybrid VAWT has a similar static torque variation to the single Savonius. The static torque is positive at most phase positions except $50° - 69°$. So, the hybrid VAWT can self-start at most positions.

B. Power performance

Regarding the hybrid VAWT, advantages are taken from two types of single rotors in the way of starting up easily and maintaining as high power as a single Darrieus. However, the presence of Savonius

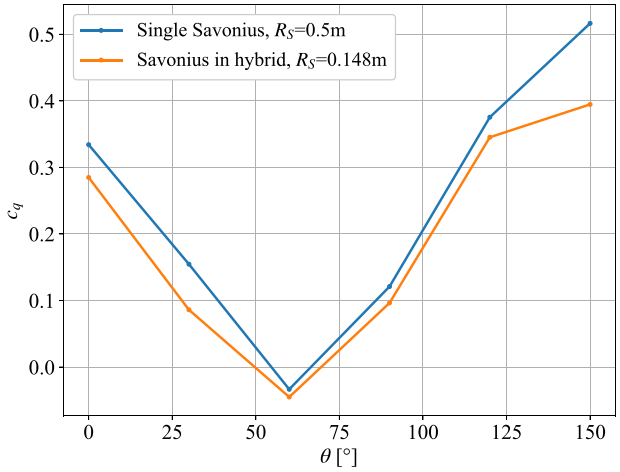

FIG. 9. Static torque coefficient of single Savonius and Savonius in hybrid VAWT.

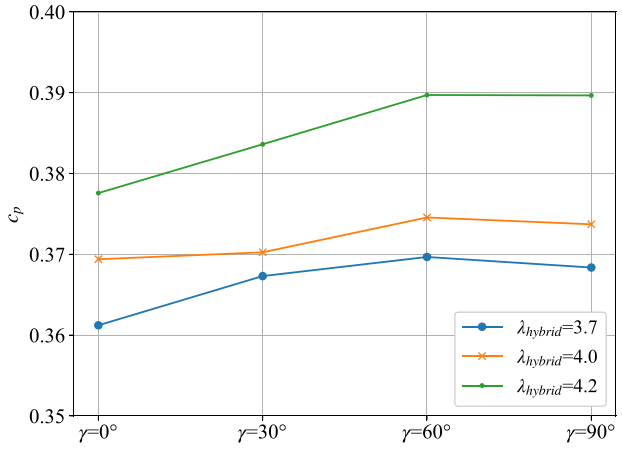

FIG. 10. Effect of λ_{hybrid} on the power coefficient of hybrid VAWT, $\frac{R_D}{R_S} = 5$.

in hybrid VAWT would suppress power generation.[21] This section aims to find out the correlation between torque variation and vortex dynamics with varied attachment angle and Savonius' tip speed ratio (varied Savonius' rotation speed) in one revolution.

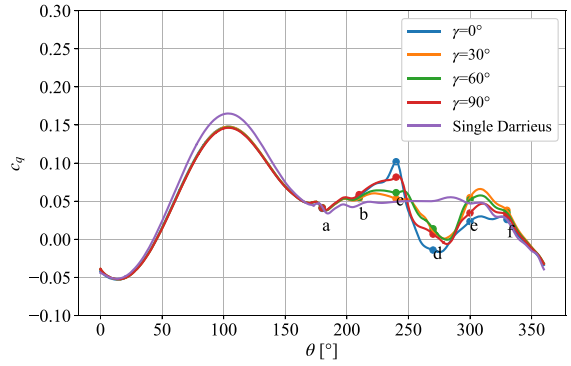

(a) Darrieus blade in hybrid turbine

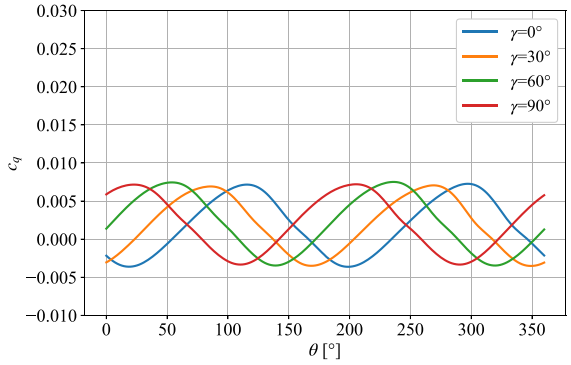

(b) Savonius blade in hybrid turbine

FIG. 11. Effect of the attachment angle on the torque generation of Darrieus and Savonius blades, $\lambda_{hybrid} = \lambda_D = 4$, $\frac{R_D}{R_S} = 5$. (a) Darrieus blade in a hybrid turbine, (b) Savonius blade in a hybrid turbine.

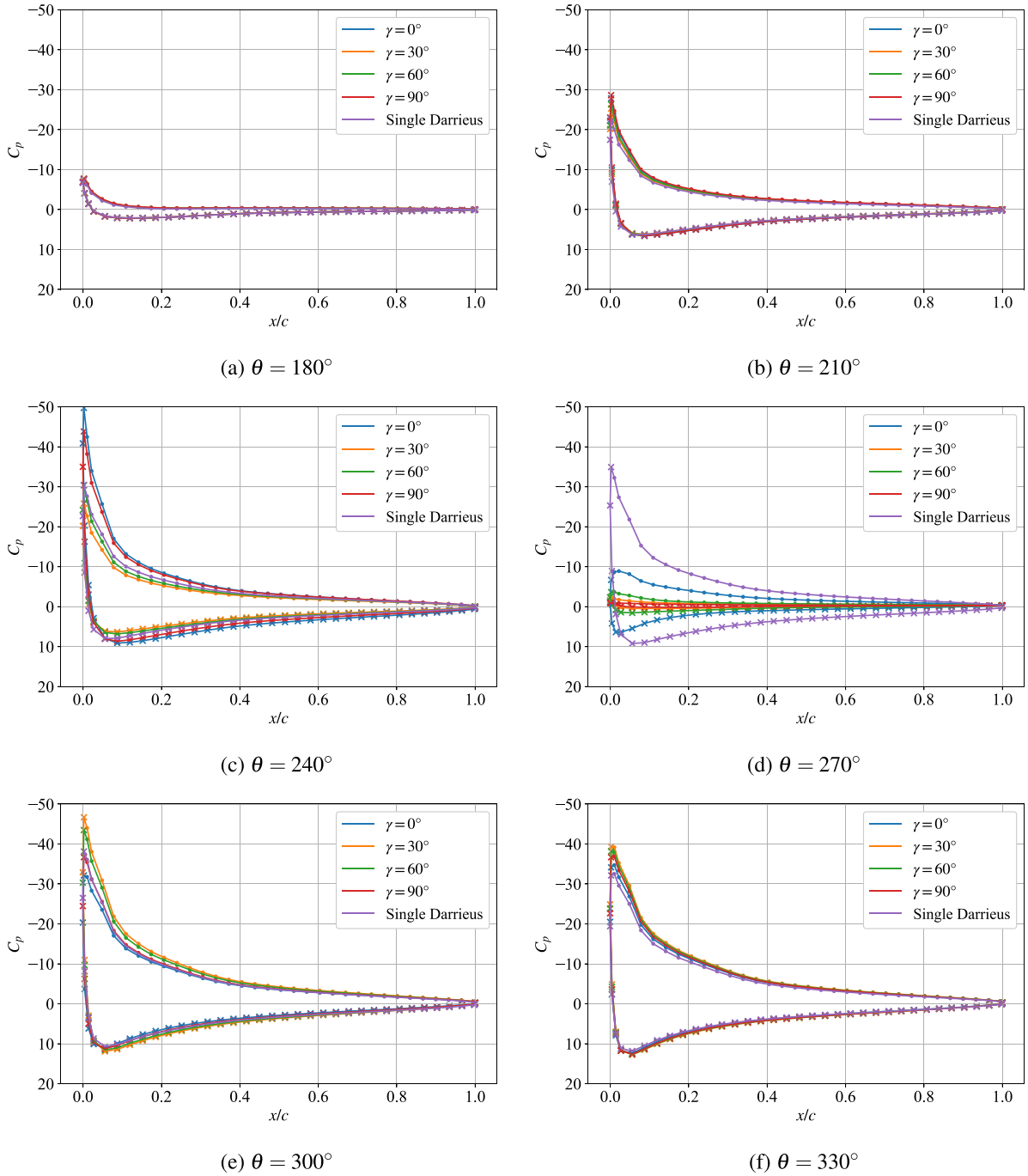

(a) $\theta = 180^\circ$ (b) $\theta = 210^\circ$

(c) $\theta = 240^\circ$ (d) $\theta = 270^\circ$

(e) $\theta = 300^\circ$ (f) $\theta = 330^\circ$

FIG. 12. Effect of the attachment angle on the pressure distribution along the Darrieus blade, $\lambda_{hybrid} = \lambda_D = 4$, $\frac{R_0}{R_s} = 5$, (a) $\theta = 180^\circ$, (b) $\theta = 210^\circ$, (c) $\theta = 240^\circ$, (d) $\theta = 270^\circ$, (e) $\theta = 300^\circ$, and (f) $\theta = 330^\circ$.

1. Effect of attachment angle

To understand the vortex dynamics effects on the blade forces, a detailed blade–vortex interaction study is conducted in this section. The interaction scheme between Savonius' wake and Darrieus blade is varied by the attachment angle. The power coefficients of hybrid VAWT with four attachment angles are depicted in Fig. 10 at three tip speed ratios. It is observed that hybrid VAWT with $\gamma = 60^\circ$ and 90°

generates a relatively high power coefficient regardless of the tip speed ratio.

Taking an example of $\lambda_{hybrid} = 4.0$, the torque contributions of the Darrieus and Savonius blades in the hybrid VAWT are discussed below. The effect of the attachment angle on the torque generation of the Darrieus and Savonius blades is shown in Fig. 11. It is observed that the torque variation trend of the Savonius blade in hybrid VAWT shows very little variation in different attachment angles, while that of the Darrieus blade in hybrid VAWT is highly distinguished at $\theta = 180^\circ - 360^\circ$. The presence of the Savonius reduces the upwind Darrieus blade torque in hybrid VAWT due to the blockage effect. The torque coefficient in $\gamma = 0^\circ$ decreases from 0.10 to −0.013 in 30°. Its gradient ($\frac{0.10+0.013}{30} = 0.0038$) is larger than the other three cases, which are 0.0022, 0.0016, and 0.0013 for $\gamma = 90^\circ$, 60°, and 30°, respectively. In addition, the difference between the maximum and the minimum torque coefficients in the second-half rotation of $\gamma = 0^\circ$ is the highest among the four cases. The rapid variation of the blade forces occurring in the second-half rotation may cause fatigue loads for the Darrieus blade.

To study the effects of the attachment angle on the blade forces and correlate the vortex dynamics to the blade forces, the pressure distributions along the blade surface and the vorticity fields at different phase angles are depicted in Figs. 12 and 15, respectively. The difference between maximum and minimum pressure coefficients on the Darrieus blade is denoted by ΔC_p. Its variation with attachment angles is shown in Fig. 13. Through the analysis of pressure distribution and vorticity field at $\theta = 180^\circ$, 210°, and 330° (denoted by phases a, b, and f), blade 1 is not significantly affected by the perturbed region due to the presence of the Savonius part, so the pressure distributions and pressure differences slightly vary with the attachment angles. It indicates that the attachment angle shows little effect on the torque when the Darrieus blade is outside of the Savonius' wake region. This also indicates the benefits of the large radius ratio to the power performance of the hybrid VAWT. In Fig. 11(a), it is observed that the torque coefficient of the Darrieus blade in the hybrid VAWT increases with the phase angle ranging from $\theta = 180^\circ$ to $\theta = 240^\circ$. The pressure fields of the single Darrieus and hybrid VAWT at $\theta = 210^\circ$ are shown in Fig. 14. The low-pressure region at the outer side of the Darrieus blade in hybrid VAWT is larger than that in single Darrieus. The increasing size of the low-pressure region at the outer side of the Darrieus blade is attributed to the vortex flow behind the Savonius rotor. The torque is observed to increase from $\theta = 180^\circ$ to $\theta = 240^\circ$ in Fig. 11(a), which can be attributed to the rotation of the Darrieus blade from the high-pressure region to the low-pressure region (Savonius' wake region).

At $\theta \approx 240^\circ$ (phase c), blade 1 rotates into the shed vortex from the advanced Savonius blade. For $\gamma = 0^\circ$ and 90°, the leading edge of blade 1 is approaching the shed vortex from the advanced Savonius blade. In Figs. 12(c) and 13, the pressure differences of $\gamma = 0^\circ$ and 90° at $\theta = 240^\circ$ are larger than ΔC_p of single Darrieus, leading to a higher torque generation compared to the single Darrieus. The pressure differences at $\gamma = 30^\circ$ and 60° are lower than the single Darrieus, but their torque coefficients are still higher than the single Darrieus. It is worth noting that forces and moments are output in their total and constituent components in OpenFOAM.[29] In this work, the sum of pressure and viscous contributions to moments is equal to the blade torque. Because blade 1 interacts with the shed vortex of Savonius

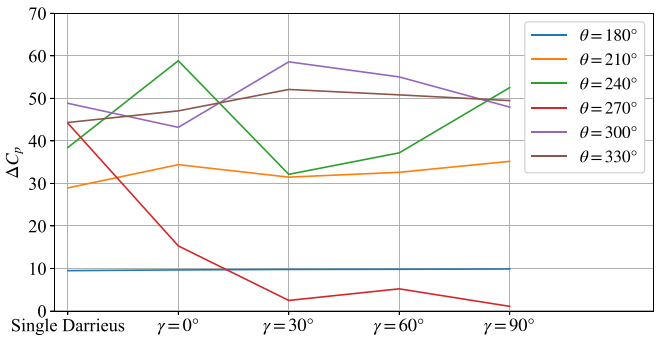

FIG. 13. Variation of pressure difference with varied attachment angles at different phases, $\Delta C_p = C_{p_{max}} - C_{p_{min}}$.

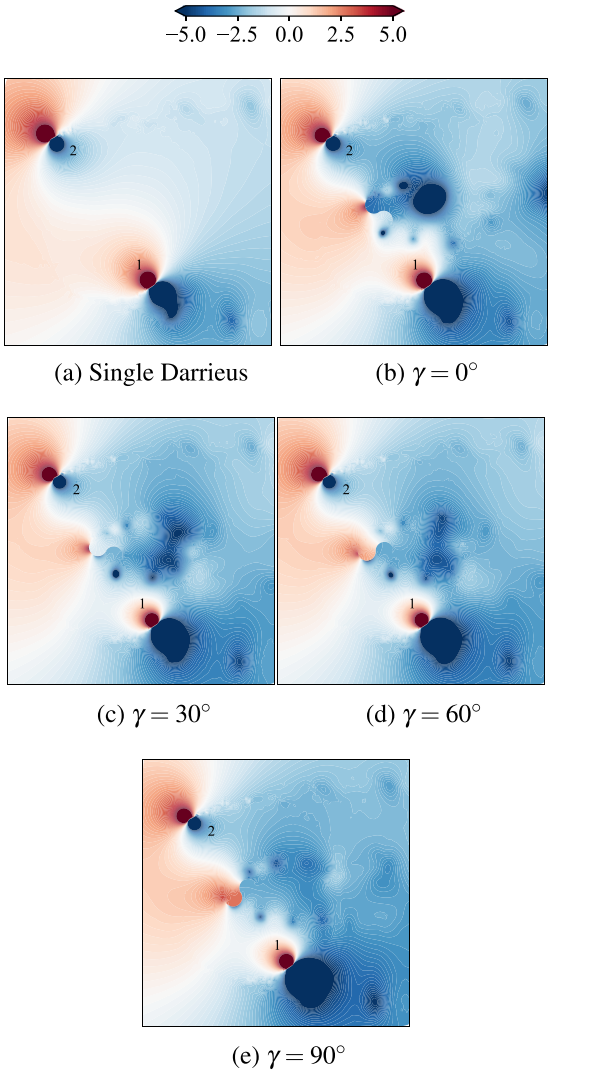

FIG. 14. Pressure fields of the single Darrieus and hybrid VAWT at $\theta = 210^\circ$: (a) single Darrieus, (b) $\gamma = 0^\circ$, (c) $\gamma = 30^\circ$, (d) $\gamma = 60^\circ$, and (e) $\gamma = 90^\circ$.

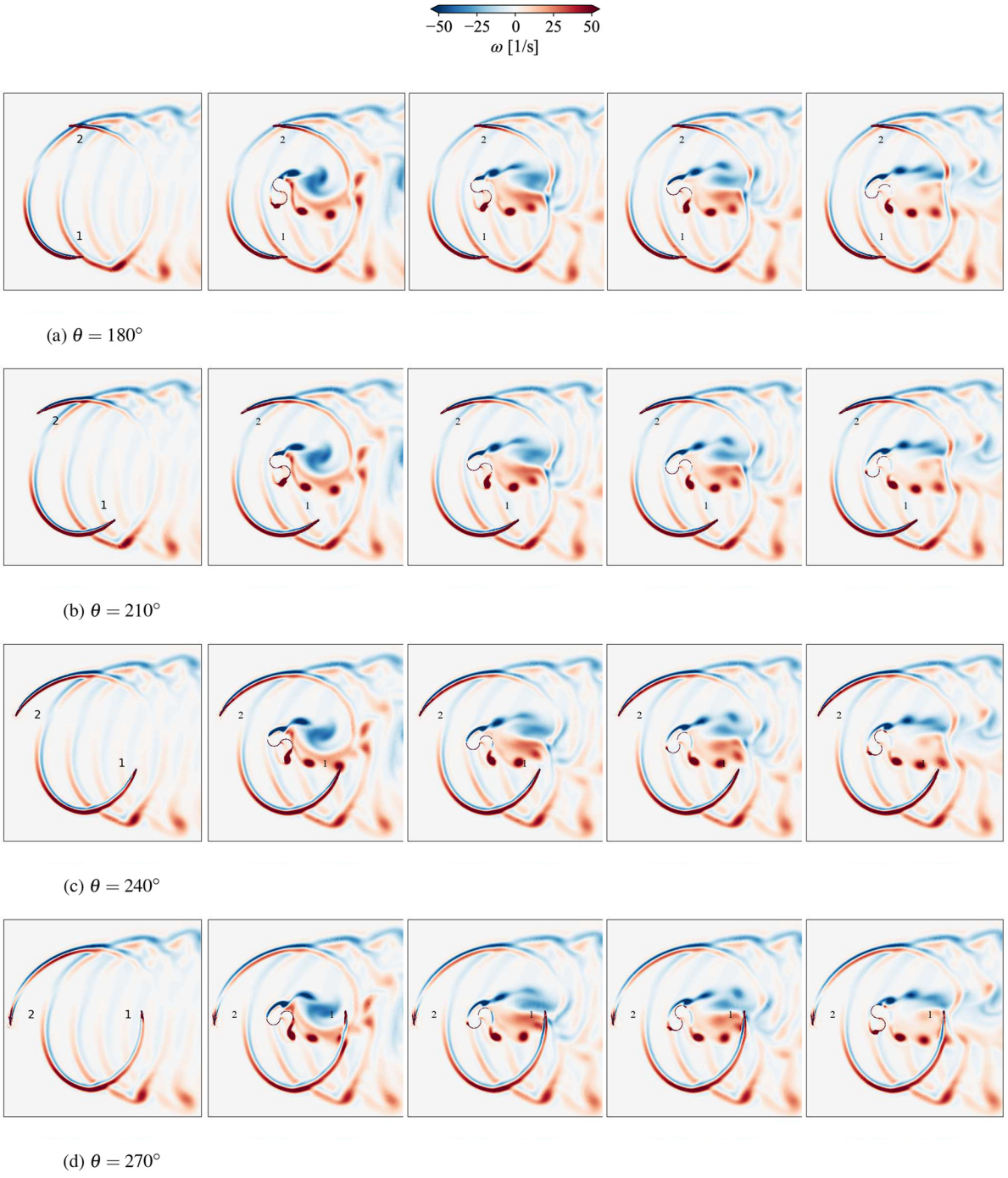

FIG. 15. Effect of γ on vorticity fields at six phase angles, $\lambda_{hybrid} = 4$, $\lambda_S = 0.8$, $\frac{R_D}{R_S} = 5$: (a) $\theta = 180°$, (b) $\theta = 210°$, (c) $\theta = 240°$, (d) $\theta = 270°$, (e) $\theta = 300°$, and (f) $\theta = 330°$ (Left to right: Single Darrieus, $\gamma = 0°$, $\gamma = 30°$, $\gamma = 60°$, $\gamma = 90°$).

directly at $\gamma = 0°$ and $90°$ as shown in Fig. 15(c), where the pressure contribution dominates the torque generation. While blade 1 at $\gamma = 30°$ and $60°$ cannot directly interact with shed vortices, in which case the viscous contribution dominates the torque generation.

After $\theta = 240°$ (after phase c), blade 1 goes through the large separated region behind the Savonius, where the Darrieus blade has a strong interaction with the Savonius' wake and a significant velocity deficit. Compared to the single Darrieus case, less power can be

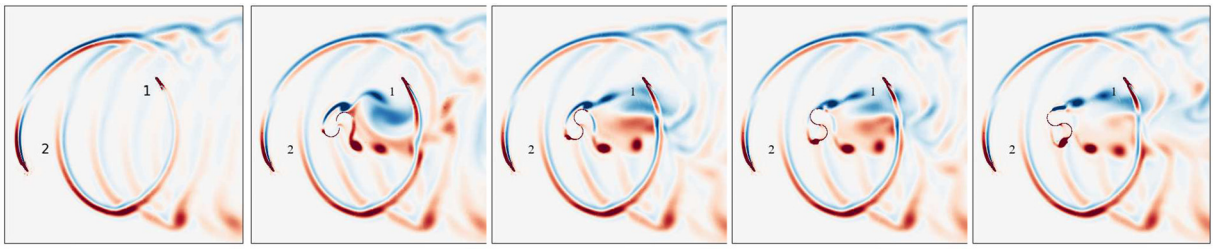

(e) $\theta = 300°$

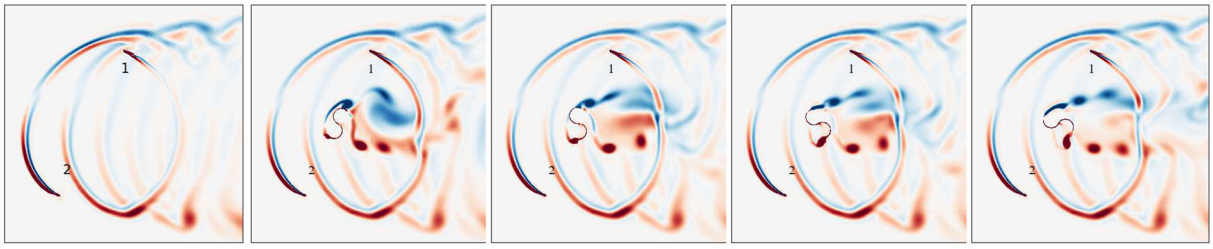

(f) $\theta = 330°$

FIG. 15. (*Continued.*)

converted by the rotor.[10] At $\theta = 270°$ (phase d), the pressure coefficients and the adverse pressure gradient at the leading edge decrease as the attachment angle increases. In Fig. 13, the pressure difference of the hybrid VAWT is lower compared to the single Darrieus. At this phase, the Darrieus blade torque drops to a certain amount and experiences a subsequent increase due to the flow perturbances of Savonius. It is observed that blade 1 interacts with the shed vortices from the two Savonius blades at $\gamma = 30° - 90°$. This interaction between blade 1 and wake makes the flow around the blade more perturbed so that the flow near the blade internal side differs much from the external side, in which case the pressure contribution dominates the torque generation. This leads to a torque decrease with the pressure difference decrease. The torque generation at $\gamma = 30° - 90°$ is more than $\gamma = 0°$, but the pressure differences of the former three cases are lower than that of the latter case because blade 1 is situated in between the shed vortices from the advancing and advanced Savonius blades in the case of $\gamma = 0°$ where viscous contribution dominates the torque generation. So, the attachment angle of $30° - 90°$ can be used as a flow control guide to reduce power losses from downstream blades of the hybrid VAWT.

At $\theta = 300°$ (phase e), blade 1 is rotating out of the Savonius wake disturbances. The shed vortex from the advancing Savonius blade appears on the internal side of blade 1, and the pressure difference between the internal and the external sides of blade 1 increases compared to $\theta = 270°$ (phase d). The torque coefficient of blade 1 at phase e yields a higher magnitude than that at phase d. In Fig. 15(e), for cases where $\gamma = 30°$ and 60°, blade 1 is notably influenced to a greater extent by the nearby shed vortices originating from the advancing Savonius blade in comparison to cases where $\gamma = 0°$ and 90°. The pressure differences and torque coefficients at $\gamma = 30°$ and 60° are higher, and the Darrieus blades have higher adverse pressure gradients compared to those at $\gamma = 0°$ and 90°.

Overall, the toque generations of the four attachment angles at $\theta = 240°$ and 210° are higher compared to the single Darrieus blade, shown in Fig. 11. Therefore, the shed vortex from the advanced Savonius blade increases the torque generation. This dependency of the torque increase on the shed vortex from the advanced Savonius blade is observed in various attachment angle cases.

TABLE VI. Power coefficient of hybrid VAWT with different rotation speeds of Savonius, $\lambda_{hybrid} = 4.0$, $\gamma = 0°$.

	$\lambda_S = 0.2$	$\lambda_S = 0.4$	$\lambda_S = 0.6$	$\lambda_S = 0.8$
$c_{p_{hybrid}}$	0.400 07	0.389 82	0.384 62	0.369 38

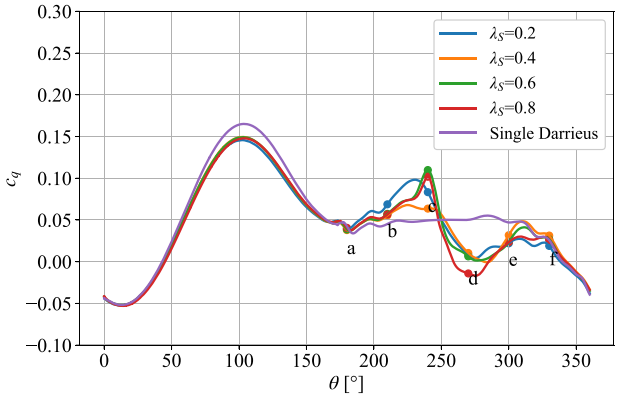

FIG. 16. Effect of Savonius' tip speed ratio on torque variation of the top Darrieus blade in hybrid VAWT and single Darrieus, $\lambda_{hybrid} = \lambda_D = 4$ ($\gamma = 0°$, $\lambda_S = \frac{\Omega_S R_S}{U_\infty}$).

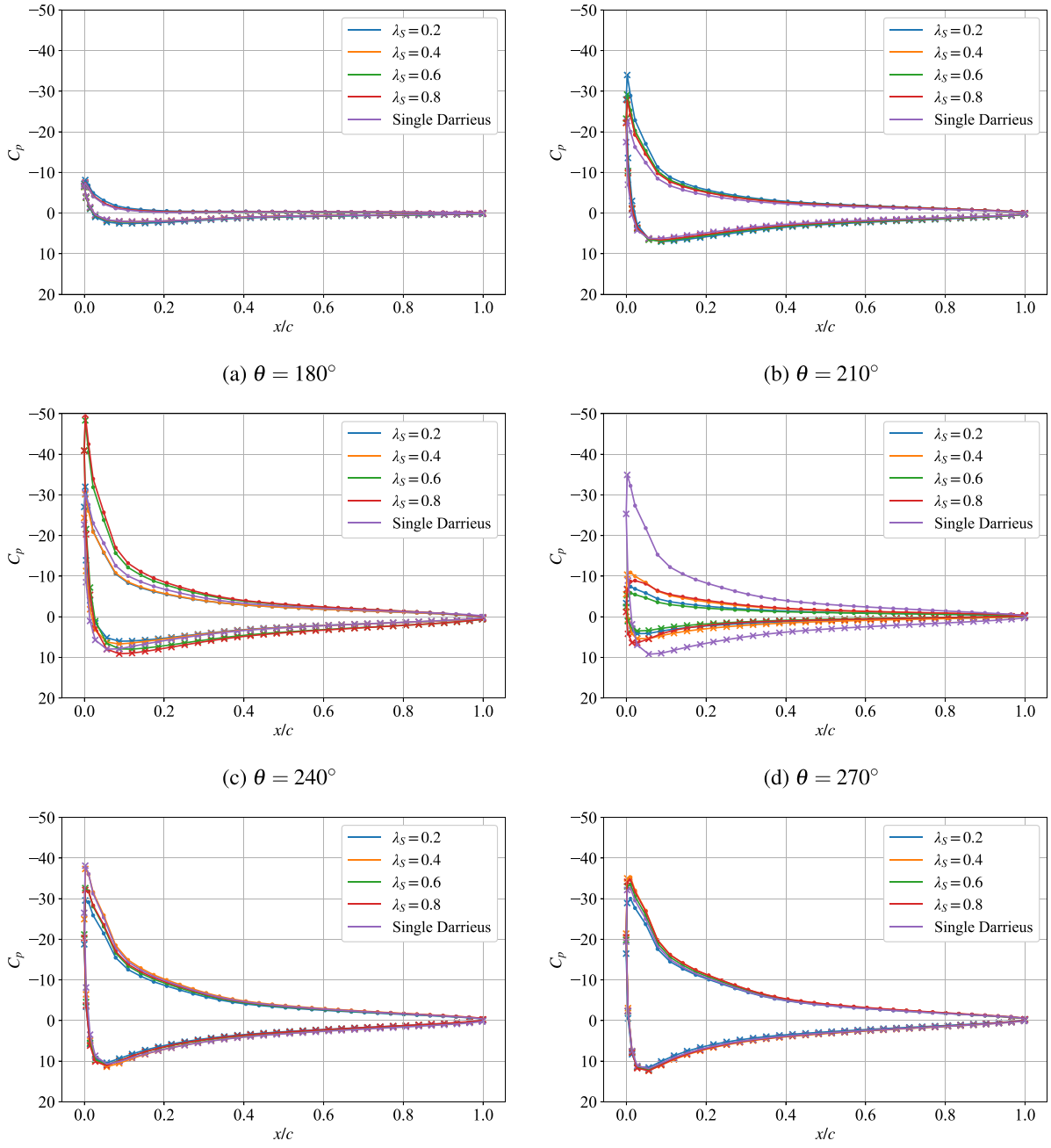

FIG. 17. Effect of λ_S on the pressure distribution along the Darrieus blade, $\lambda_{Hybrid} = \lambda_D = 4$, $\frac{R_D}{R_S} = 5$: (a) $\theta = 180°$, (b) $\theta = 210°$, (c) $\theta = 240°$, (d) $\theta = 270°$, (e) $\theta = 300°$, and (f) $\theta = 330°$.

2. Effect of Savonius' rotation speed

As the inner Savonius perceives a lower incoming flow during the rotation of the hybrid VAWT, the equivalent tip speed ratio for Savonius is different from the original tip speed ratio. To study the effect of Savonius' rotation on the hybrid VAWT, Savonius and Darrieus are assumed to be mounted in separate rotation axes. The relation between the original tip speed ratio and the power coefficient of the hybrid VAWT is shown in Table VI. It shows a slight power increase for the case with a lower λ_S. Therefore, slowing down the

inner Savonius after start-up is beneficial for the power performance of the hybrid VAWT. Reducing the size of the inner Savonius leads to the same effect, but it is difficult to achieve during turbine operation. Apart from the mean power of the hybrid VAWT, the torque variation during rotation is also analyzed.

The torque variations of blade 1 in hybrid VAWT and single Darrieus are compared in Fig. 16. The force fluctuation in the second-half revolution is investigated. The torque coefficient at $\lambda_S = 0.8$ has the most rapid change compared to the other three cases. This is due to the large shedding frequency of Savonius's wake. So, there is a higher possibility of the occurrence of fatigue. From $\theta = 180^\circ$ to $\theta = 240^\circ$, the same trends of torque increase as the varied γ cases are observed due to the blade rotation from high-pressure region to low-pressure region (Savonius' wake region).

To analyze flow physics in the second-half revolution of hybrid VAWT with varied λ_S, six angular positions from 180° to 330° are denoted by phases a to f. The pressure distribution along the blade surface, the pressure difference between the maximum and minimum values, and the vorticity field around the rotor at the six phases are shown in Figs. 17–19, respectively. The torque coefficients of blade 1 in the single Darrieus rotor at $\theta = 180^\circ$ and 330° (phases a and f) are similar to those in the hybrid VAWT when varying the rotation speed of the inner Savonius because blade 1 only interacts with the wake shedding from the Darrieus blades, with no disturbances introduced from the Savonius wake. At $\theta = 210^\circ$ (phase b), blade 1 rotates toward the shed vortex shed from the advanced Savonius blade tip. As the size of the shed vortex blob grows with the decreasing rotation speed, the pressure difference between the internal and external sides of blade 1 and its torque coefficient at $\lambda_S = 0.2$ is higher compared to that at $\lambda_S = 0.4$–0.6. At $\theta = 240^\circ$ (phase c) $\lambda_S = 0.6$ and 0.8, the shed vortex from the advanced Savonius blade appears at the internal side of blade 1, resulting in a stronger adverse pressure gradient and larger pressure difference at the leading edge. The torque generation is also higher than $\lambda_S = 0.2$ and 0.4.

At $\theta = 270^\circ$ (phase d), blade 1 is behind the Savonius and experiences a large velocity deficit. The pressure difference between the internal and external sides of the leading edge reduces, leading to the reduction of torque generation. $\lambda_S = 0.8$ has more power losses than the other cases due to Savonius' high induction to the flow field. So, reducing the rotation speed of the inner Savonius would decrease the power losses downstream. Compared to the single Darrieus, the pressure differences of blade 1 in hybrid VAWT at four Savonius' tip speed ratios are lower, shown in Figs. 17 and 18. It is observed that the pressure difference decreases on the order of single Darrieus, $\lambda_S = 0.4$, $\lambda_S = 0.8$, $\lambda_S = 0.2$, $\lambda_S = 0.6$, but the blade torque decreased on the order of single Darrieus, $\lambda_S = 0.4$, $\lambda_S = 0.2$, $\lambda_S = 0.6$, $\lambda_S = 0.8$. The outlier $\lambda_S = 0.8$ may be because the pressure contribution cannot dominate the blade torque generation. At $\theta = 300^\circ$ (phase e), blade 1 rotates outward of the shed vortex from the advancing Savonius blade. At $\lambda_S = 0.4$, the near vortex has a bigger impact on blade 1 compared to the other Savonius' tip speed ratios, leading to the highest ΔC_p and c_q at $\theta = 300^\circ$.

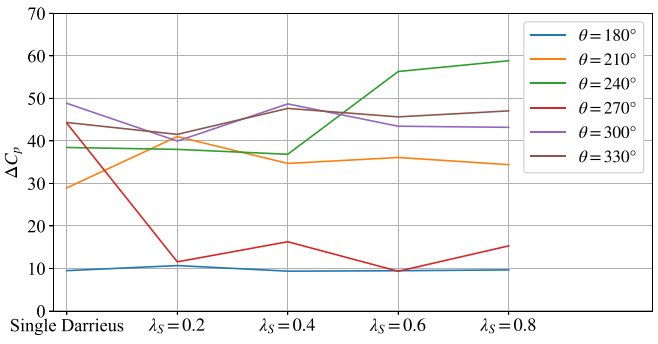

FIG. 18. Variation of pressure difference with varied Savonius' tip speed ratios at different phases, $\Delta C_p = C_{p_{max}} - C_{p_{min}}$.

IV. CONCLUSIONS

The effects of the attachment angle and Savonius' rotation speed on the blade–vortex interaction and performances of a hybrid VAWT have been thoroughly investigated in the present paper. The studies were conducted employing a computational fluid dynamic approach. Four attachment angles for the hybrid VAWT and four rotation speeds for the inner Savonius have been evaluated systematically. Several conclusions can be drawn from the paper:

(1) The two-bladed Savonius without the gap distance can self-start at most phase angles except 50° − 69°.
(2) At $\gamma = 60^\circ$ and 90°, the power coefficient of the hybrid VAWT is larger compared to 0° and 30°.
(3) In the downwind part, the torque variation is dependent on the blade–vortex interaction. The torque coefficient of the Darrieus blade in hybrid VAWT is higher than that in the single Darrieus, while the blade interacts with the shed vortex from the advanced Savonius blade. This dependency is observed in varied attachment angles and varied tip speed ratio cases.
(4) The effect of Savonius' rotation on the performance of the hybrid VAWT is studied. The results indicate that slowing down the Savonius in hybrid VAWT leads to less induction to the flow field and more available energy downstream. Lower λ_S is beneficial to the power performance of the Darrieus part in the hybrid VAWT regardless of the complex mechanics of the rotation axis.
(5) From $\theta = 180^\circ$ to 240°, the blade torque increases with the increasing phase angle because the Darrieus blade rotates from high-pressure region to low-pressure region (Savonius' wake region), leading to the torque increase in the rotation direction.
(6) When the Darrieus blade does not interact directly with shed vortices, e.g., blade 1 is situated in between vortices at $\theta = 270^\circ$, $\lambda_S = 0.8$, the viscous contribution would dominate the torque generation.
(7) A rapid force variation occurs when the Darrieus blade interacts with the Savonius' wake. The Darrieus blade in hybrid VAWT with $\gamma = 0^\circ$ and $\lambda_S = 0.8$ has the largest gradient of force drop, which might lead to fatigue for the hybrid VAWT.

From the power and start-up performance point of view, it is suggested to apply an attachment angle of 60° or 90°, and low λ_S of 0.2 to improve the rotor performance.

Exploring blade–vortex interactions in Darrieus–Savonius combined vertical axis wind turbines offers a promising research avenue. By characterizing flow patterns and linking them with blade torque variations, we gain insights that can improve turbine performance. This study illuminates the complex vortex dynamics that shape the behavior of the hybrid VAWT, guiding design enhancements and operational strategies. These insights inform design improvements and operational strategies, advancing both theoretical understanding and

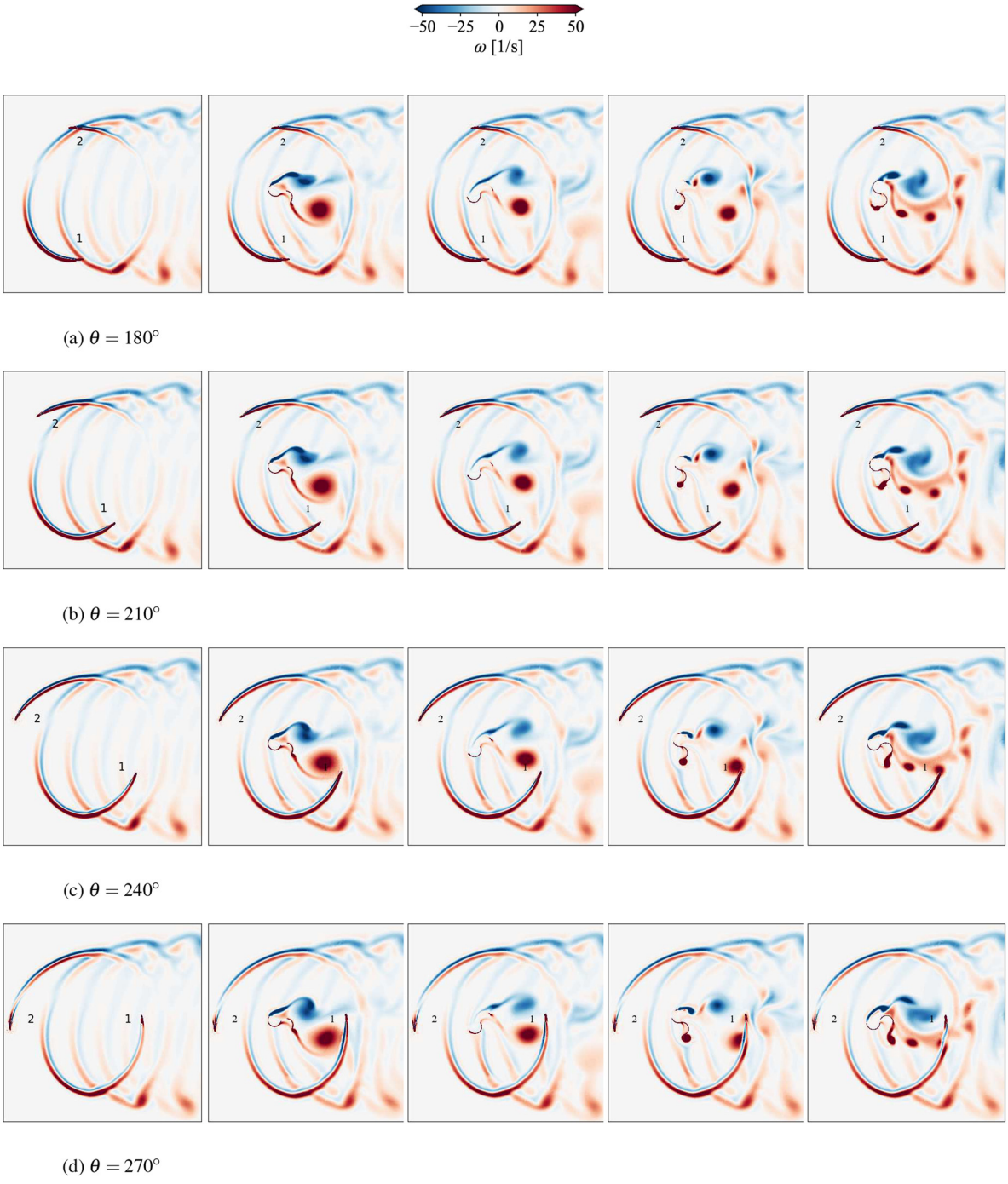

FIG. 19. Effect of λ_S on vorticity fields at six phase angles, $\lambda_{hybrid} = 4$, $\gamma = 0°$, $\frac{R_D}{R_S} = 5$: (a) $\theta = 180°$, (b) $\theta = 210°$, (c) $\theta = 240°$, (d) $\theta = 270°$, (e) $\theta = 300°$, and (f) $\theta = 330°$ (Left to right: Single Darrieus, $\lambda_S = 0.2$, $\lambda_S = 0.4$, $\lambda_S = 0.6$, $\lambda_S = 0.8$).

practical renewable energy solutions. This study uses 2 D simulation. To extend the comprehensive study of vortex dynamics in hybrid VAWT, 3 D effects can be taken into account in future work. The studied baseline hybrid VAWT will be validated against published experimental results. It may not be the optimal case, but the correlation of vortex dynamics and blade torque can provide preliminary insights to improve its performance. A parametric study can be conducted to further extend this work. Different rotation speeds of

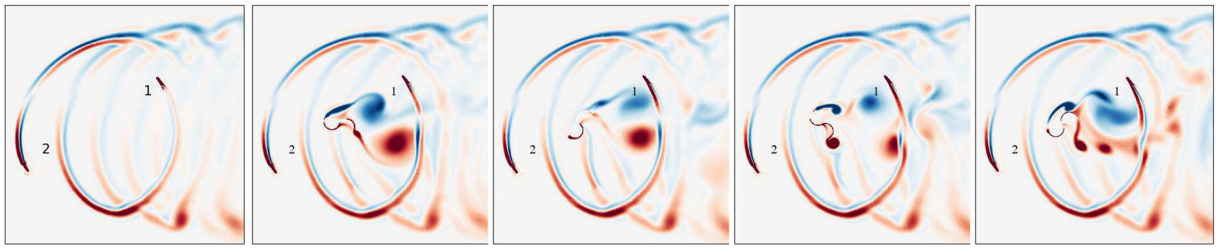

(e) $\theta = 300°$

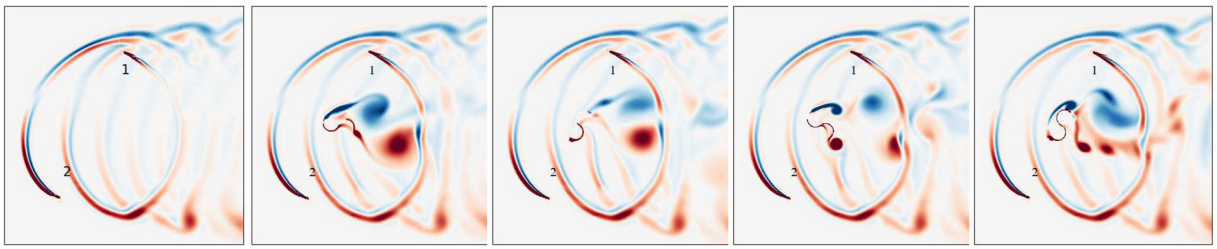

(f) $\theta = 330°$

FIG. 19. (*Continued.*)

Darrieus and Savonius parts increase the complexity of the design for the rotation axis of the hybrid VAWT. Investigating the design approach for the rotation axis of the hybrid VAWT would facilitate the control of the Savonius component's operation, enabling adjustments to enhance the start-up and power performances of the hybrid VAWT.

ACKNOWLEDGMENTS

Jingna Pan gratefully acknowledges financial support from China Scholarship Council (Grant No. 201906450032).

AUTHOR DECLARATIONS

Conflict of Interest

The authors have no conflicts to disclose.

Author Contributions

Jingna Pan: Conceptualization (equal); Formal analysis (equal); Investigation (equal); Methodology (equal); Validation (equal); Visualization (equal); Writing – original draft (equal); Writing – review & editing (equal). **Carlos J. Ferreira:** Conceptualization (equal); Project administration (equal); Supervision (equal); Writing – review & editing (equal). **Alexander van Zuijlen:** Conceptualization (equal); Project administration (equal); Supervision (equal); Writing – review & editing (equal).

DATA AVAILABILITY

The data that support the findings of this study are available from the corresponding author upon reasonable request.

NOMENCLATURE

2D	Two-dimensional
3D	Three-dimensional
AMI	Arbitrary mesh interface
CFD	Computational fluid dynamics
C_p	Pressure coefficient
c_p	Power coefficient
$c_{p_{max}}$	Peak power coefficient
c_q	Torque coefficient
e	Gap width
k	Turbulent kinetic energy
PIMPLE	PISO-SIMPLE
PISO	Pressure Implicit with Splitting of Operators
p	Pressure
R_1	Semi-major axis of the elliptic Savonius blade
R_2	Semi-minor axis of the elliptic Savonius blade
R_D	Darrieus rotor radius
R_{hybrid}	Radius of hybrid VAWT
R_S	Savonius rotor radius
SIMPLE	Semi-Implicit Method for Pressure Linked Equations
SST	Shear stress transport
TSR	Tip speed ratio
URANS	Unsteady Reynolds-averaged Navier–Stokes
U_∞	Inflow velocity
u	Sum of the mean velocity and the fluctuating velocity
u_τ	Friction velocity
VAWT	Vertical axis wind turbine
w	Turbulent dissipation rate
x	Coordinate in the horizontal axis
y	Coordinate in the vertical axis

γ	Attachment angle
ΔC_p	Difference of maximum and minimum pressure coefficients
Δy_1	Distance between the cell and the nearest wall
ε	Overlap ratio of Savonius blades
θ	Phase angle
λ_{hybrid}	Tip speed ratio of hybrid VAWT
λ_{max}	Maximum tip speed ratio of the rotor
λ_{min}	Minimum tip speed ratio of the rotor
λ_S	Tip speed ratio of Savonius
μ	Dynamic viscosity
μ_t	Turbulent viscosity
υ	Kinematic viscosity
ρ	Flow density
Φ	Arc angle of the Savonius blade
Ω	Rotational speed
ω	Vorticity

APPENDIX A: MESH INDEPENDENCE STUDY OF SAVONIUS

The mesh independence study is conducted to determine the appropriate mesh size for OpenFOAM simulations of VAWT. A single-stage two-bladed semicircular Savonius rotor without gap width[23] is arranged in a computational domain of $30R_S \times 50R_S$. The distance between the inlet and the Savonius rotation axis is $15R_S$. The inflow wind speed is 7 m/s with a corresponding rotation speed of 11.2 rad/s. Three sets of meshing with varying mesh resolutions were generated with the first row's cell height of 0.046, 0.051, and 0.056 mm and the growth factor of 1.2. In this study, the first row's cell height was calculated with the premise of the dimensionless wall distance $y^+ = \frac{\rho u_\tau \cdot \Delta y_1}{\mu}$[39] lower than one. The three sets of mesh are named coarse mesh, medium mesh, and fine mesh, with the total numbers of mesh being around 1.77×10^5, 1.83×10^5, and 1.90×10^5 and blade discretization of 296, 312, and 332, respectively. Pave meshing scheme is applied for all surfaces. The discretization of the inlet and outlet boundaries uses a double-sided successive ratio of 0.95 to refine the wake region. The maximum values of the calculated y^+ occur at the convex side of blades with an average value below one. This indicates an effective meshing strategy.[40] The power coefficients from the three mesh configurations are shown in Table VII. The values of the maximum skewness for the three mesh configurations are 0.72, 0.73, and 0.66, respectively. The medium and coarse mesh configurations differ by 0.15% and 0.57% from the fine mesh, which indicates that the medium mesh yields reasonably accurate results. In order to properly control convergence, the simulation residual was set as 1×10^{-5}. Among all the simulations in this work, the interpolation scheme has a second order of accuracy. The azimuthal increment of 0.24°/ step was chosen according to the published time step independence study for a Savonius rotor with a similar tip speed ratio, wind speed, and diameter.[41,42] The simulation time is over 12 revolutions. The power coefficients of Savonius from different revolutions are shown in Fig. 20. It demonstrates that there is little change in the power coefficient between the sixth and seventh revolutions. So, the simulation results are considered as converged from the sixth revolution.

TABLE VII. Power coefficient of Savonius rotor from different mesh configurations, $\lambda_S = 0.8$, $U_\infty = 7$ m/s.

Mesh	Fine	Medium	Coarse
Number of cells	1.90×10^5	1.83×10^5	1.77×10^5
Blade discretization	332	312	296
First row's cell height (mm)	0.056	0.051	0.046
Number of layers	26	28	30
Power coefficient c_p	0.2614	0.2618 (+0.15%)	0.2629 (+0.57%)

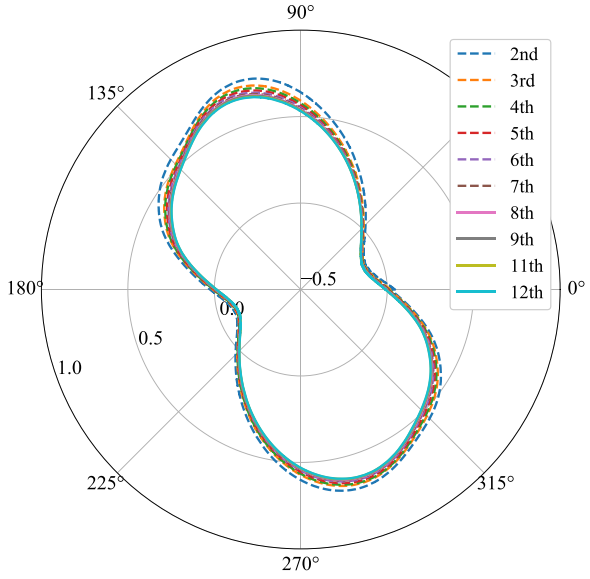

FIG. 20. Convergence of power coefficient for the Savonius rotor at 0.24°/ step, $\lambda_S = 0.8$, $U_\infty = 7$ m/s, medium mesh configuration.

APPENDIX B: MESH INDEPENDENCE STUDY OF DARRIEUS

A mesh independence study of a two-bladed Darrieus rotor with the same geometrical parameter as the Darrieus part in the hybrid VAWT and the same meshing strategy as the Savonius rotor is conducted. The rotation axis of the Darrieus rotor is $10R_D$ from the inlet and $24R_D$ from the outlet. To optimize the limits of cell size, three mesh configurations (coarse, medium, fine) are simulated with cell numbers of 1.38×10^5, 1.58×10^5, and 2.02×10^5, respectively. The values of the maximum skewness for the three mesh configurations are 0.71, 0.69, and 0.51, respectively. The simulation residual is set as 1×10^{-5}. An azimuthal increment of 0.24°/step is seen as sufficient according to the convergence studies of Rezaeiha *et al.*[43] and Edwards *et al.*[44] The average $y+$ over the blade surface is below one with the maximum value at the leading edge.[40] The power coefficients from different mesh configurations and mesh details are shown in Table VIII. The convergence of the power coefficient from different revolutions is depicted in Fig. 21. The results

TABLE VIII. Power coefficient of the Darrieus rotor from different mesh configurations, $\lambda_D = 4.0$, $U_\infty = 4.01$ m/s.

Mesh	Fine	Medium	Coarse
Number of cells	2.02×10^5	1.58×10^5	1.38×10^5
Blade discretization	92	70	62
First row's cell height (mm)	0.018	0.022	0.018
Number of layers	28	28	30
Power coefficient c_p	0.4343	0.4220 (−2.83%)	0.3604 (−17.0%)

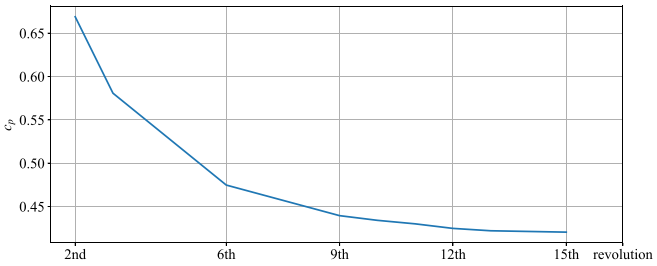

FIG. 21. Convergence of power coefficient for the Darrieus rotor at 0.24°/step, $\lambda_D = 4.0$, $U_\infty = 4.01$ m/s, medium mesh configuration.

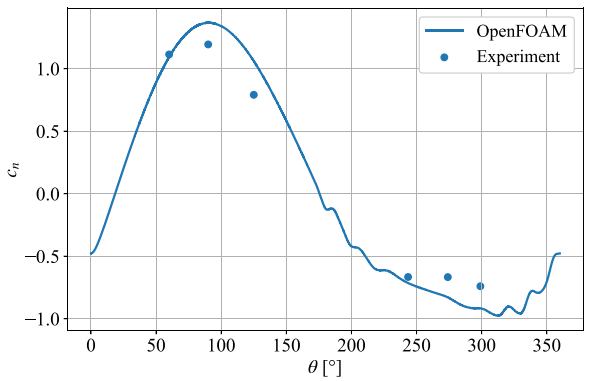

FIG. 22. Comparison of numerical and experimental normal force coefficients of the Darrieus blade.

show that the medium mesh configuration yields reasonably accurate results with a −2.83% difference from the fine mesh configuration. The power coefficient of the Darrieus rotor is seen as converged from the twelfth revolution. The normal force coefficient of the single Darrieus is validated against the experimental results,[30] shown in Fig. 22. The results indicate a comparable agreement between the numerical and experimental results.

REFERENCES

[1]A. Hosseini and N. Goudarzi, "Design and CFD study of a hybrid vertical-axis wind turbine by employing a combined Bach-type and h-Darrieus rotor systems," Energy Convers. Manage. **189**, 49–59 (2019).
[2]D. W. Wekesa, C. O. Saoke, and J. N. Kamau, "An experimental investigation into performance characteristics of h-shaped and Savonius-type VAWT rotors," Sci. Afr. **10**, e00603 (2020).
[3]H. Fatahian, Z. Mohamed-Kassim, and W. S. Chang, "Insights into the flow dynamics and rotor performance of a Savonius turbine with dynamic venting using controllable flaps," Phys. Fluids **34**, 127109 (2022).
[4]M. R. Castelli, G. Ardizzon, L. Battisti, E. Benini, and G. Pavesi, "Modeling strategy and numerical validation for a Darrieus vertical axis micro-wind turbine," in *Proceedings of ASME International Mechanical Engineering Congress and Exposition* (ASME, 2010), Vol. 44441, pp. 409–418.
[5]Y. Wang, X. Sun, X. Dong, B. Zhu, D. Huang, and Z. Zheng, "Numerical investigation on aerodynamic performance of a novel vertical axis wind turbine with adaptive blades," Energy Convers. Manage. **108**, 275–286 (2016).
[6]R. Gosselin, G. Dumas, and M. Boudreau, "Parametric study of H-Darrieus vertical-axis turbines using CFD simulations," J. Renewable Sustainable Energy **8**, 053301 (2016).
[7]Y. Shao, J. Su, Y. Tu, L. Kuang, Z. Han, K. Zhang, and D. Zhou, "Assessment of the aerodynamic benefits of collocating horizontal- and vertical-axis wind turbines in tandem using actuator line model," Phys. Fluids **35**, 075115 (2023).
[8]X. Liang, S. Fu, B. Ou, C. Wu, C. Y. Chao, and K. Pi, "A computational study of the effects of the radius ratio and attachment angle on the performance of a Darrieus–Savonius combined wind turbine," Renewable Energy **113**, 329–334 (2017).
[9]X. Sun, Y. Chen, Y. Cao, G. Wu, Z. Zheng, and D. Huang, "Research on the aerodynamic characteristics of a lift drag hybrid vertical axis wind turbine," Adv. Mech. Eng. **8**(1), 1–11 (2016).
[10]A. Pallotta, D. Pietrogiacomi, and G. P. Romano, "Hybri – A combined Savonius–Darrieus wind turbine: Performances and flow fields," Energy **191**, 116433 (2020).
[11]N. R. Maldar, C. Y. Ng, and E. Oguz, "A review of the hybrid Darrieus–Savonius turbine for hydrokinetic applications," in *Proceedings of 2021 Third International Sustainability and Resilience Conference: Climate Change* (IEEE, 2021), pp. 424–431.
[12]J. Sarma, S. Jain, P. Mukherjee, and U. K. Saha, "Hybrid/combined Darrieus–Savonius wind turbines: Erstwhile development and future prognosis," J. Sol. Energy Eng. **143**, 050801 (2021).
[13]A. Roshan, A. Sagharichi, and M. J. Maghrebi, "Nondimensional parameters' effects on hybrid Darrieus–Savonius wind turbine performance," J. Energy Resour. Technol. **142**(1), 011202 (2020).
[14]M. Asadi and R. Hassanzadeh, "Effects of internal rotor parameters on the performance of a two bladed Darrieus-two bladed Savonius hybrid wind turbine," Energy Convers. Manage. **238**, 114109 (2021).
[15]Y. Kyozuka, "An experimental study on the Darrieus–Savonius turbine for the tidal current power generation," J. Fluid Sci. Technol. **3**, 439–449 (2008).
[16]G. Bangga, S. Hutani, and H. Heramarwan, "The effects of airfoil thickness on dynamic stall characteristics of high-solidity vertical axis wind turbines," Adv. Theory Simul. **4**, 2000204 (2021).
[17]Y. Wang, S. Shen, G. Li, D. Huang, and Z. Zheng, "Investigation on aerodynamic performance of vertical axis wind turbine with different series airfoil shapes," Renewable Energy **126**, 801–818 (2018).
[18]P. Kumar, M. Surya, K. Sivalingam, T.-C. Lim, S. Ramakrishna, and W. He, "Computational optimization of adaptive hybrid Darrieus turbine: Part 1," Fluids **4**, 90 (2019).
[19]A. Tripathi, P. Das, T. Aggarwal *et al.*, "Efficiency enhancement of a hybrid vertical axis wind turbine by utilizing optimum parameters," Mater. Today: Proc. **62**, 3582–3588 (2022).
[20]E. Maican, L. Dumitrescu, R. Radot, O. Ciobanu, and D. Preda, "Analysis and optimization of a Savonius-Darrieus hybrid wind turbine," Ann. Fac. Eng. Hunedoara **19**, 151–156 (2021), see https://www-proquest-com.tudelft.idm.oclc.org/scholarly-journals/analysis-optimization-savonius-darrieus-hybrid/docview/2568718968/se-2.
[21]K. Liu, M. Yu, and W. Zhu, "Enhancing wind energy harvesting performance of vertical axis wind turbines with a new hybrid design: A fluid-structure interaction study," Renewable Energy **140**, 912–927 (2019).
[22]G. Saini and R. Saini, "A numerical analysis to study the effect of radius ratio and attachment angle on hybrid hydrokinetic turbine performance," Energy Sustainable Dev. **47**, 94–106 (2018).

[23]J. Pan, C. Ferreira, and A. van Zuijlen, "Estimation of power performances and flow characteristics for a Savonius rotor by vortex particle method," Wind Energy **26**, 76–97 (2023).
[24]N. Franchina, G. Persico, and M. Savini, "2d-3d computations of a vertical axis wind turbine flow field: Modeling issues and physical interpretations," Renewable Energy **136**, 1170–1189 (2019).
[25]L. Chao, Z. Sonye, X. You-Lin, and X. Yiqing, "2.5 d large eddy simulation of vertical axis wind turbine in consideration of high angle of attack," Renewable Energy **51**, 317–330 (2013).
[26]N. Alom and U. K. Saha, "Examining the aerodynamic drag and lift characteristics of a newly developed elliptical-bladed Savonius rotor," J. Energy Resour. Technol. **141**, 051201 (2019).
[27]F. Li, J. Yao, C. Eskilsson, Y. Pan, J. Chen, and R. Ji, "Investigations on the wave performance of Savonius turbine operating under initial phase-locked strategy," Phys. Fluids **35**, 097138 (2023).
[28]C. Vigneswaran and G. VishnuKumar, "Computational analysis of influence of CFJ components on aerodynamic performance," Phys. Fluids **35**, 093619 (2023).
[29]OpenFOAM, *OpenFOAM User Guide* (2017).
[30]B. LeBlanc and C. Ferreira, "Estimation of blade loads for a variable pitch vertical axis wind turbine from particle image velocimetry," Wind Energy **25**, 313–332 (2022).
[31]C. D. Argyropoulos and N. Markatos, "Recent advances on the numerical modelling of turbulent flows," Appl. Math. Modell. **39**, 693–732 (2015).
[32]S. Aftab, A. Mohd Rafie, N. Razak, and K. Ahmad, "Turbulence model selection for low reynolds number flows," PLoS One **11**, e0153755 (2016).
[33]F. R. Menter, "Two-equation eddy-viscosity turbulence models for engineering applications," AIAA J. **32**, 1598–1605 (1994).
[34]F. R. Menter, M. Kuntz, R. Langtry *et al.*, "Ten years of industrial experience with the SST turbulence model," Heat Mass Transfer **4**, 625–632 (2003), see https://citeseerx.ist.psu.edu/document?repid=rep1&type=pdf&doi=107feacb716406055c7aba4bddc3a6e8337c21c1.
[35]D. C. Wilcox, "Reassessment of the scale-determining equation for advanced turbulence models," AIAA J. **26**, 1299–1310 (1988).
[36]D. Wilcox, *Turbulence Modeling for CFD*, 3rd ed. (DCW Industries, 2006).
[37]B. F. Blackwell, L. V. Feltz, and R. E. Sheldahl, "Wind tunnel performance data for two-and three-bucket Savonius rotors," Technical Report No. SAND-76-0131, Sandia Laboratories Springfield, VA, USA, 1977.
[38]M. H. M. Yazik, W. S. Chang, M. H. H. Ishak, E. Fatahian, and F. Ismail, "Effect of surface roughness and blade material on the performance of a stationary Savonius wind turbine under different operating conditions," Phys. Fluids **35**, 035133 (2023).
[39]H. Versteeg and W. Malalasekera, *An Introduction to Computational Fluid Dynamics: The Finite Volume Method* (Pearson Education Limited, 2007).
[40]E. Fatahian, A. L. Nichkoohi, H. Salarian, and J. Khaleghinia, "Comparative study of flow separation control using suction and blowing over an airfoil with/without flap," Sādhanā **44**, 220 (2019).
[41]P. Jaohindy, S. McTavish, F. Garde, and A. Bastide, "An analysis of the transient forces acting on savonius rotors with different aspect ratios," Renewable Energy **55**, 286–295 (2013).
[42]S. McTavish, D. Feszty, and T. Sankar, "Steady and rotating computational fluid dynamics simulations of a novel vertical axis wind turbine for small-scale power generation," Renewable Energy **41**, 171–179 (2012).
[43]A. Rezaeiha, I. Kalkman, and B. Blocken, "CFD simulation of a vertical axis wind turbine operating at a moderate tip speed ratio: Guidelines for minimum domain size and azimuthal increment," Renewable Energy **107**, 373–385 (2017).
[44]J. M. Edwards, L. A. Danao, and R. J. Howell, "PIV measurements and CFD simulation of the performance and flow physics and of a small-scale vertical axis wind turbine," Wind Energy **18**, 201–217 (2015).